coatings

Article

Effect of WC Content on the Wear and Corrosion Properties of Oscillating Laser-Cladding-Produced Nickel-Based Coating

Xuening Li [1], Songyan Zhang [1], Wei Liu [1], Xiaotong Pang [1], Yonggang Tong [1], Mingjun Zhang [1], Jian Zhang [1] and Kaiming Wang [1,2,*]

1 College of Automotive and Mechanical Engineering, Changsha University of Science and Technology, Changsha 410114, China
2 State Key Laboratory of Tribology in Advanced Equipment, Department of Mechanical Engineering, Tsinghua University, Beijing 100084, China
* Correspondence: kmwang@csust.edu.cn

Abstract: Pneumatic conveying pipe is an important part of the coal industry. Its working environment is harsh, and it is mainly affected by serious wear and corrosion, which affects its operating life. Studying a method of strengthening the pipe wall of pneumatic conveying pipe is of great significance. In this paper, nickel-based alloy coatings with different WC (tungsten carbide) contents were prepared using an oscillating laser-cladding process, and the micro-characterization characteristics, wear resistance and corrosion resistance of the laser-cladded layer were discussed. The main conclusions are as follows: The microstructure of the laser-cladded layer gradually grows from the plane crystals and cellular crystals at the bottom to the relatively coarse columnar crystals in the middle, and finally to a large number of equiaxed crystals in the upper part. Moreover, with an increase in WC content, more fine equiaxed crystals are formed, mainly due to the decrease in temperature gradient with the increase in distance from the fusion line. Also, with an increase in WC content, the hardness and wear resistance of the nickel-based alloy are improved. When 20% WC is added, the laser-cladded layer shows the best corrosion resistance in 3.5 wt.% NaCl solution, and its polarization resistance is 16% lower than that when 10% WC is added. This study provides a technical reference for improving the operating life of pneumatic conveying pipelines.

Keywords: oscillating laser cladding; WC content; nickel-based coating; wear resistance; corrosion resistance

Citation: Li, X.; Zhang, S.; Liu, W.; Pang, X.; Tong, Y.; Zhang, M.; Zhang, J.; Wang, K. Effect of WC Content on the Wear and Corrosion Properties of Oscillating Laser-Cladding-Produced Nickel-Based Coating. *Coatings* **2023**, *13*, 1614. https://doi.org/10.3390/coatings13091614

Academic Editor: Michał Kulka

Received: 29 July 2023
Revised: 28 August 2023
Accepted: 12 September 2023
Published: 15 September 2023

1. Introduction

Coal has always been the backbone of China's energy structure, with its coal industry being a global leader and ranking third in the world. The coal industry is an important economic sector that is crucial to the national economy and a significant component of national economic development. An efficient underground transportation system is an essential part of coal mining, as it ensures operational safety, improves efficiency, and reduces production costs [1]. Currently, pneumatic conveying through pipelines has been widely used as a safe, clean, and environmentally friendly method for transporting coal powder and small particles. However, it should be noted that during the transportation of particles along the pneumatic pipeline, the scraping effect of the material and the erosion of the corrosive material, as well as improper pipeline design, can cause significant wear at the bends of the pipeline due to changes in the direction of movement, leading to severe damage [2]. Additionally, pipelines used for pneumatic conveying are prone to corrosion due to their prolonged exposure to a humid environment, resulting in seal failures and significantly affecting the service life of the pipelines [3].

Laser cladding is a novel surface-enhancement technique that forms a coating with specific properties on the surface of the substrate material [4–6]. By adjusting the parameters, the density and shape of the coating can be controlled, thereby improving aspects of performance of the coated surface, such as wear resistance, corrosion resistance, and thermal stability [7–9]. Compared to other traditional surface-treatment techniques, such as thermal spraying and surfacing welding, laser cladding offers advantages such as a high cooling rate, low dilution rate, low deformation, dense microstructure, wide selection of alloy powders, and good flexibility [10–12]. It has found applications in various industries such as aerospace, automotive, marine, chemical, electronics, medical, and high-end manufacturing [13,14]. Ning et al. [15] used underwater wire-feeding laser-cladding technology to prepare an in situ laser-cladded layer of nickel–aluminum bronze directly in the water environment. A local dry cavity was generated by the self-designed underwater laser-cladding nozzle to protect the cladding area from the water environment. Hu et al. [16] utilized laser cladding to deposit a nickel-based WC composite powder on the surface of a TBM cutter ring, aiming to prolong the service life of the cutter. The presence of spherical WC particles, as well as decomposed WC and W_2C small particles, effectively hindered the pressing and ploughing of hard rock particles, thus improving the tribological properties of the TBM cutter ring. Shi et al. [17] prepared a coating on the surface of brake discs by employing laser cladding with nickel-based alloy powders. By comparing the amount of wear before and after the coating, it was found that the coating exhibited superior wear resistance. These results indicate that laser-cladded nickel-based coating is an effective means to enhance the tribological performances of brake discs. This research shows that laser cladding has become an important process in the field of surface repair and processing.

In order to improve wear resistance and corrosion resistance, a new method involves adding reinforcing particles into nickel-based coatings. Currently, ceramic particle (such as TiC, SiC, etc.)-reinforced cobalt-based [18,19], nickel-based [20,21], or Fe-based [22,23] alloy coatings prepared using laser cladding are widely used. Research on strengthening nickel-based alloy coatings with high-hardness-WC ceramic particles has also gradually emerged as a research hotspot. Wu et al. [24] established a three-dimensional finite element model of double-channel double-layer laser cladding, based on the thermophysical properties of Ni60A-25% WC powder and the design of a double-ellipsoid heat-source model. The simulation results showed that the laser power was proportional to the temperature and the residual compressive stresses in all the paths, and the scanning speed was inverse. Wu et al. [25] prepared a single Fe/WC laser-cladded layer, a composite coating of Fe/WC cladding, and a Ni60 transition coating on the surface of 60Si2Mn spring steel using a laser-cladding technology. The experimental results showed that the added Ni60 transition coating reduces the possibility of generating pores and cracks in the Fe/WC composite coating, and the diffusion of the Ni element reduces the microhardness of the laser-cladded layer and increases the average friction coefficient and wear volume of the Fe/WC-composite coating. Liu et al. [26] used laser cladding to fabricate Ni50 and Ni50-WC coatings. These results show that the addition of WC improves its microhardness, corrosion resistance and wear resistance.

The objective of this study is to improve the surface performance of pneumatic conveying pipelines through laser-cladding technology. The focus of this research is on the influence of the WC content on the microstructure characteristics, microhardness, wear resistance, and electrochemical corrosion performance of laser-cladded nickel-based coatings. The research results are expected to provide a theoretical basis and technical support for improving the surface performance of pneumatic conveying pipelines.

2. Materials and Methods

Q345R steel was chosen as the base material. Due to its excellent performance, Q345 R steel is commonly used as a material for pressure pipelines and is widely used in petroleum, chemical, mining and other industrial fields [27]. The dimensions of the specimens without surface strengthening treatment were 100 mm × 100 mm × 12 mm. The chemical composition of Q345R steel is shown in Table 1. Before conducting the laser-cladding experiment, the samples need to be polished to remove surface oxides and cleaned with anhydrous ethanol to remove impurities and oil stains from the surface of the Q345R steel. The Q345R steel substrate should be placed in a vacuum drying oven for 3 h to remove moisture.

Table 1. Chemical composition of Q345R.

C	Si	Mn	P	S	Al	Fe
≤0.20	≤0.55	1.20–1.60	≤0.025	≤0.010	≥0.020	Bal.

An Ni-based alloy powder with a particle size of 53–105 µm was selected as the laser-cladding material, and the powder was dried before the experiment for subsequent use. To further improve the wear and corrosion resistance, nickel-coated WC powder with different contents (particle size: 44–105 µm) and 0.5 wt.% of rare earth (CeO_2) were added. Different WC contents (mass ratios of 10%, 20%, 30%, and 40%) of the nickel-based alloy powder were mixed with a ball-to-powder ratio of 2:1 and placed in a ball mill. The ball-milling speed was 100 r/min, and the ball-milling time was 2 h. Depending on the WC content (10%, 20%, 30%, and 40%), the prepared Ni/WC composite powders were uniformly mixed and named D-1, D-2, D-3, and D-4, respectively.

A nickel-based alloy coating was prepared using the YLS-3000 fiber laser-cladding equipment. The laser power, laser scanning speed, and powder feeding rate were optimized based on the criteria of a defect-free characteristic and good bonding between the composite coating and substrate. Under the experimental conditions, the optimal process parameters for laser processing were determined as follows: a dual-circle oscillating pattern with an oscillating frequency of 60 Hz and an oscillating diameter of 1.5 mm, a laser power of 1000 W, a laser scanning speed of 240 mm/min, a powder feeding rate of 7 g/min, and the use of Ar gas as the shielding gas.

After laser cladding, the samples were cut into 10 mm × 10 mm × 1.5 mm cubes using spark cutting method. After grinding and polishing, metallographic samples were prepared and the samples were corroded with aqua regia (V_{HCl}:V_{HNO3} = 3:1). A scanning electron microscope (SEM, JSM-IT 200, JEOL Ltd., Tokyo, Japan) equipped with energy dispersive spectroscopy (EDS, JEOL Ltd., Tokyo, Japan) was used to observe the microstructure of the laser-cladded layer surface. Microhardness testing was performed using an HVST-1000Z semi-automatic Vickers hardness tester. A load of 200 N was applied for 15 s, and 3 sets of data were collected and averaged. Friction coefficient measurements were carried out using an MDW-05 high-frequency reciprocating wear tester. The Si_3N_4 balls with a diameter of 5 mm were selected as the grinding balls, with parameters set as follows: a frequency of 2 Hz, an axial force of 30 N, and a wear time of 30 min. Electrochemical performance testing was conducted using an electrochemical workstation. The samples were immersed in 3.5 wt.% NaCl electrolyte for 1 h, and then subjected to potentiodynamic polarization testing at a scan rate of 2 mV/s, with a polarization potential of −0.8 V_SCE for a duration of 10 min. The steady-state polarization open-circuit-potential stripping experiment was performed in the potential range of −2 V to 2 V for 30 min.

3. Results and Discussion

3.1. Microstructure

Figure 1 shows the morphology of the cross-section of the single oscillating laser-cladded layer under different WC contents. From Figure 1, it can be observed that all four groups of laser-cladded layers exhibit obvious WC particles and slight defects. Additionally, there is a distinct bright band at the interface between the laser-cladded layer and the heat-affected zone (HAZ), where the laser-cladded layer exhibits a smooth and continuous surface contour line with minimal amounts of slag [28,29], indicating a good metallurgical bond between the laser-cladded layer and the substrate.

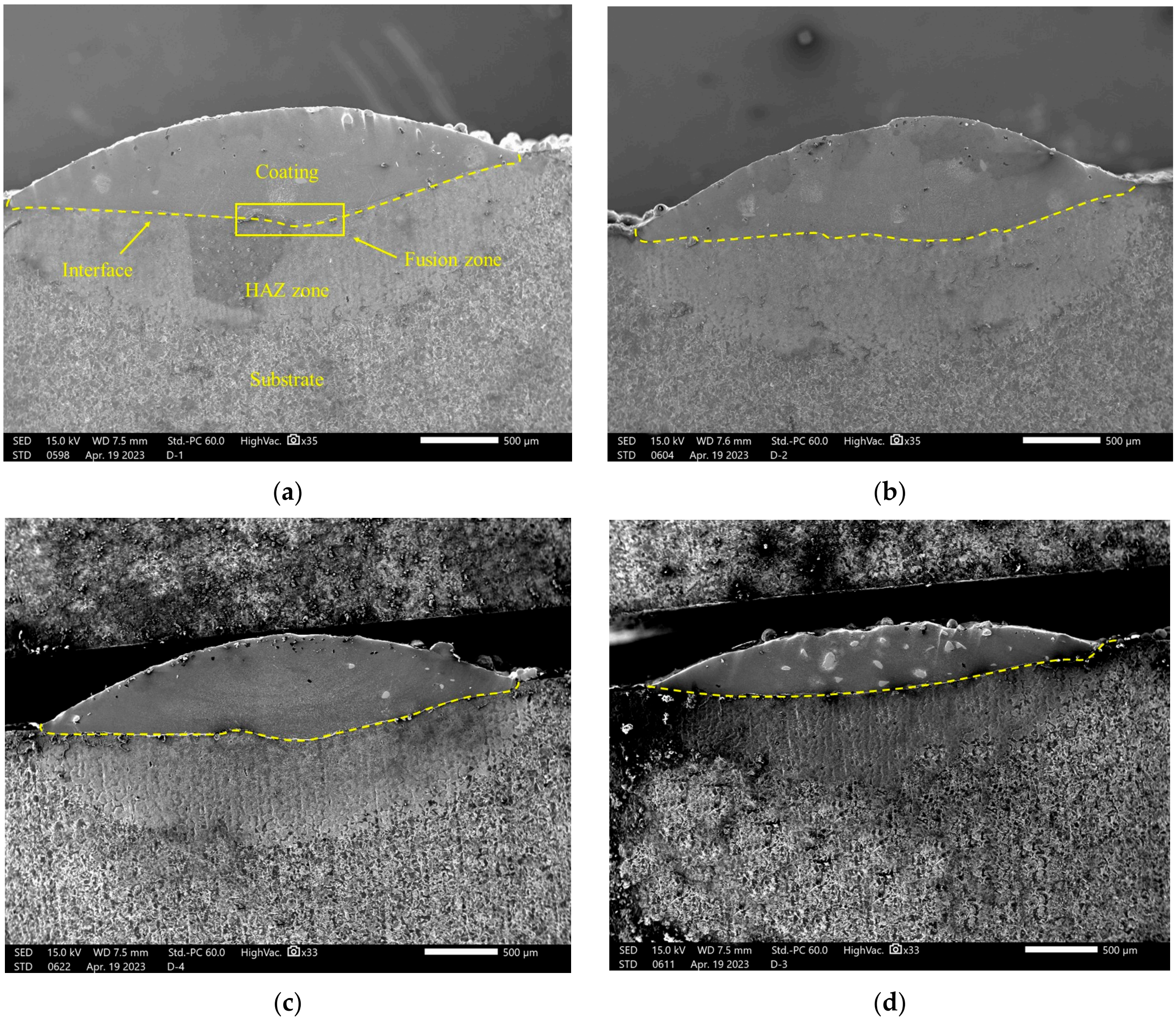

Figure 1. Morphology of laser-cladded layer cross section with different WC contents: (**a**) D1 coatings; (**b**) D2 coatings; (**c**) D3 coatings; and (**d**) D4 coatings.

The dilution rate and aspect ratio are important parameters used to evaluate the performance indicators of laser-cladded layers. The dilution rate refers to the extent of changes in the composition of the cladding alloy caused by the mixing of the melted substrate during laser cladding, which can be expressed as the percentage of the substrate alloy in the total laser-cladded layer. In general, a high dilution rate can lead to the cracking and deformation of the laser-cladded layer, while a low dilution rate can result in poor adhesion between the laser-cladded layer and the substrate, thereby affecting the overall performance of the laser-cladded layer. Therefore, the dilution rate is an important parameter to characterize the laser-cladded layer [30]. The aspect ratio refers to the ratio between the width and depth of the cladding area obtained through laser cladding, which can affect the cladding quality and efficiency. If the aspect ratio is too large or too small, it may lead to uneven or incomplete melting during the cladding process, thereby affecting the processing quality and efficiency [31]. Figure 2 shows the geometric characteristics of the cross section of the laser-cladded layer, and the calculations of the geometric dilution rate and aspect ratio are given by Equations (1) and (2).

$$\eta = \frac{h}{H+h} \times 100\% \tag{1}$$

$$\sigma = \frac{W}{H} \tag{2}$$

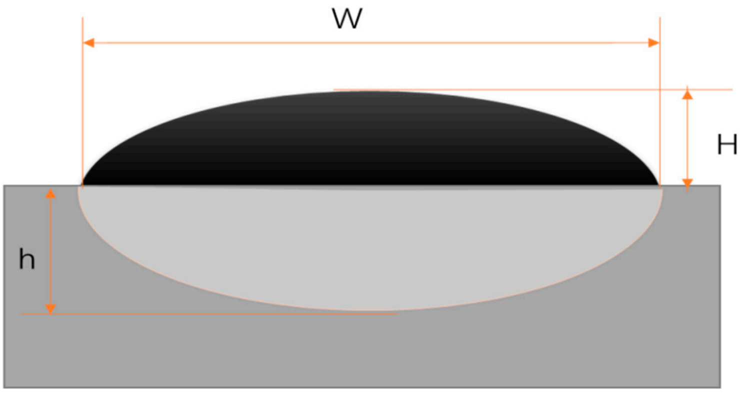

Figure 2. Laser-cladded layer cross section geometric morphology.

In the equation, η represents the dilution rate, w represents the width of the laser-cladded layer, H and h represent the height and depth of the laser-cladded layer, respectively, and σ represents the aspect ratio of the laser-cladded layer.

Subsequently, the width (w), height (H), depth (h), dilution rate (η), and aspect ratio (σ) of the laser-cladded layer were calculated based on the scale, as shown in Table 2 and Figure 3. According to the table, with the increase in WC content, the overall trend of the laser-cladded layer's height (H) and depth (h) initially increased and then decreased, while the dilution rate and aspect ratio exhibited a decreasing trend followed by an increasing trend. When the WC content was 30%, the dilution rate was at its minimum. This is because the addition of WC reduces the specific energy required for laser cladding of the same thickness coating when the WC content is low, resulting in an increase in the laser-cladded layer's height and a decrease in its depth, and thereby reducing the dilution rate [32]. However, as the WC content continues to increase, the specific energy required for laser cladding of coating of the same thickness increases, leading to a decrease in the laser-cladded layer's thickness and depth, and resulting in an increase in the dilution rate of the laser-cladded layer.

Table 2. Parameters of the laser-cladded layer.

Specimen	H/μm	h/μm	w/μm	η/%	σ
D-1	426	285.2	3283.4	40.1	7.708
D-2	622.8	321.4	3254.5	34.1	5.225
D-3	537.5	262.5	3170	32.8	5.898
D-4	305	190	3040	38.3	9.967

Figure 4 shows the microstructure of the laser-cladded layer at its interface with the substrate. From Figure 4, it can be observed that the microstructure of the laser-cladded layer changes from plane crystals and dendritic crystals near its interface with the substrate, gradually transforming into columnar crystals, and finally transitioning to equiaxed crystals in the upper region [33]. The main reason for this is the synergistic effect of the temperature gradient (G) and solidification rate (R) in determining the grain morphology [34]. During the initial stages of solidification at the interface between the laser-cladded layer and the substrate, the laser-cladding process involves rapid heating and rapid cooling. At this stage, the temperature gradient G is the largest, but the solidification rate R is the smallest, resulting in no undercooling [35]. The heat released during solidification flows entirely towards the substrate, and due to the similarity in chemical composition between the laser-cladded layer material and the substrate, there is a small surface tension at the interface, resulting in slower growth and the formation of plane crystals. As solidification progresses, the temperature gradient G at the solidification interface decreases, and the solidification rate R increases, leading to increased undercooling. At this stage, the grains have sufficient growth time, resulting in the formation of columnar crystals. The growth direction of the grains is along the heat dissipation direction, which is perpendicular to the interface between the laser-cladded layer and the substrate. As a result, columnar crystals grow in the direction perpendicular to the interface [36]. With a further increase in undercooling, i.e., a decrease in G and an increase in R, nucleation occurs not only at the solidification interface but also within the liquid metal. The distribution of nuclei is uniform, and the growth of these grains is restricted by the surrounding grains, leading to the formation of equiaxed crystals [37]. Additionally, the high thermal conductivity of WC and its dispersion within the molten pool can change the heat dissipation conditions during solidification, leading to a transformation in the overall grain morphology of the composite coating. Therefore, with an increase in WC content, the equiaxed crystals formed in the laser-cladded layer become finer and more uniform [38].

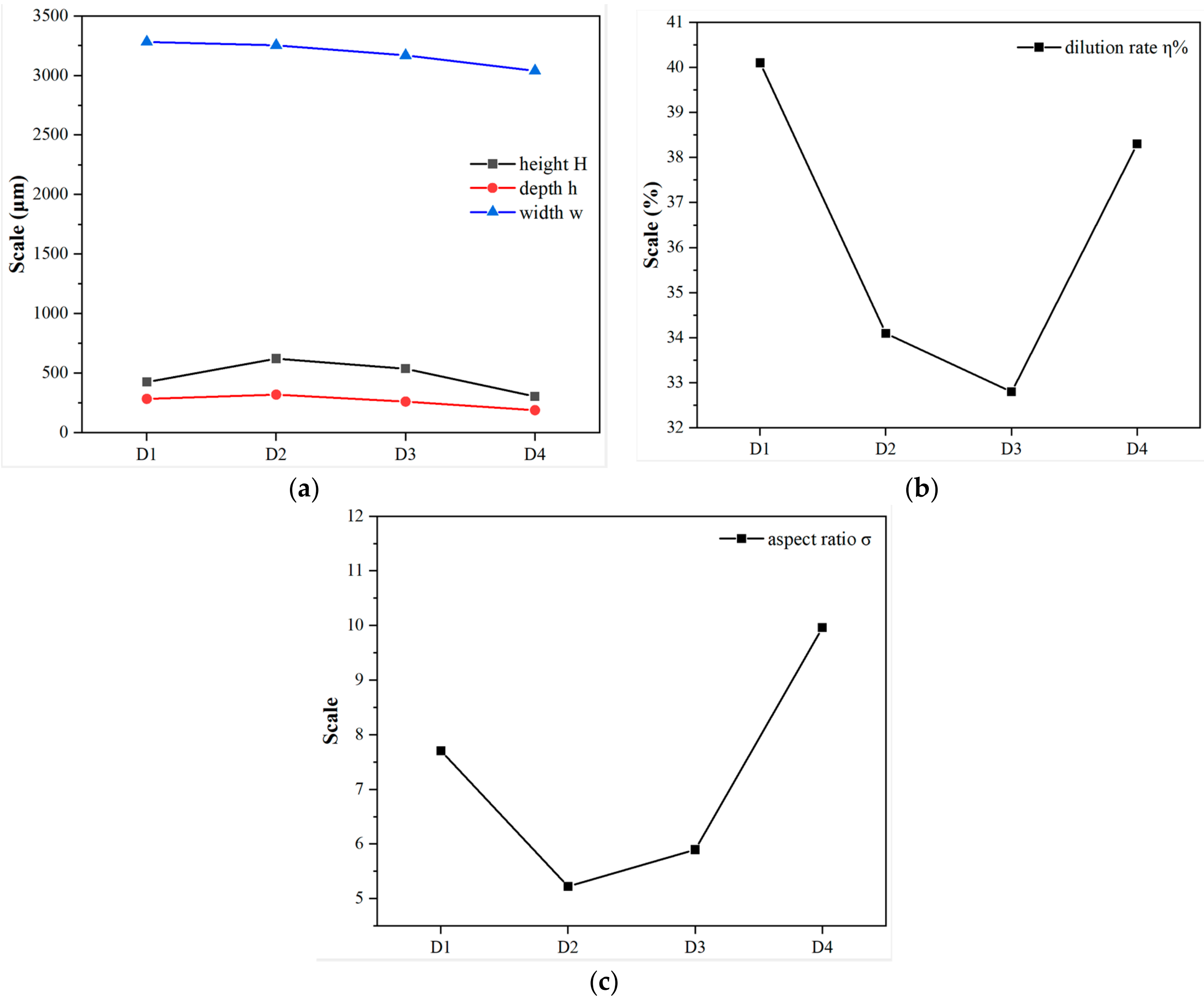

Figure 3. Line diagrams of laser-cladded layer parameters: (**a**) height H, depth h and width w; (**b**) dilution η; and (**c**) aspect ratio σ.

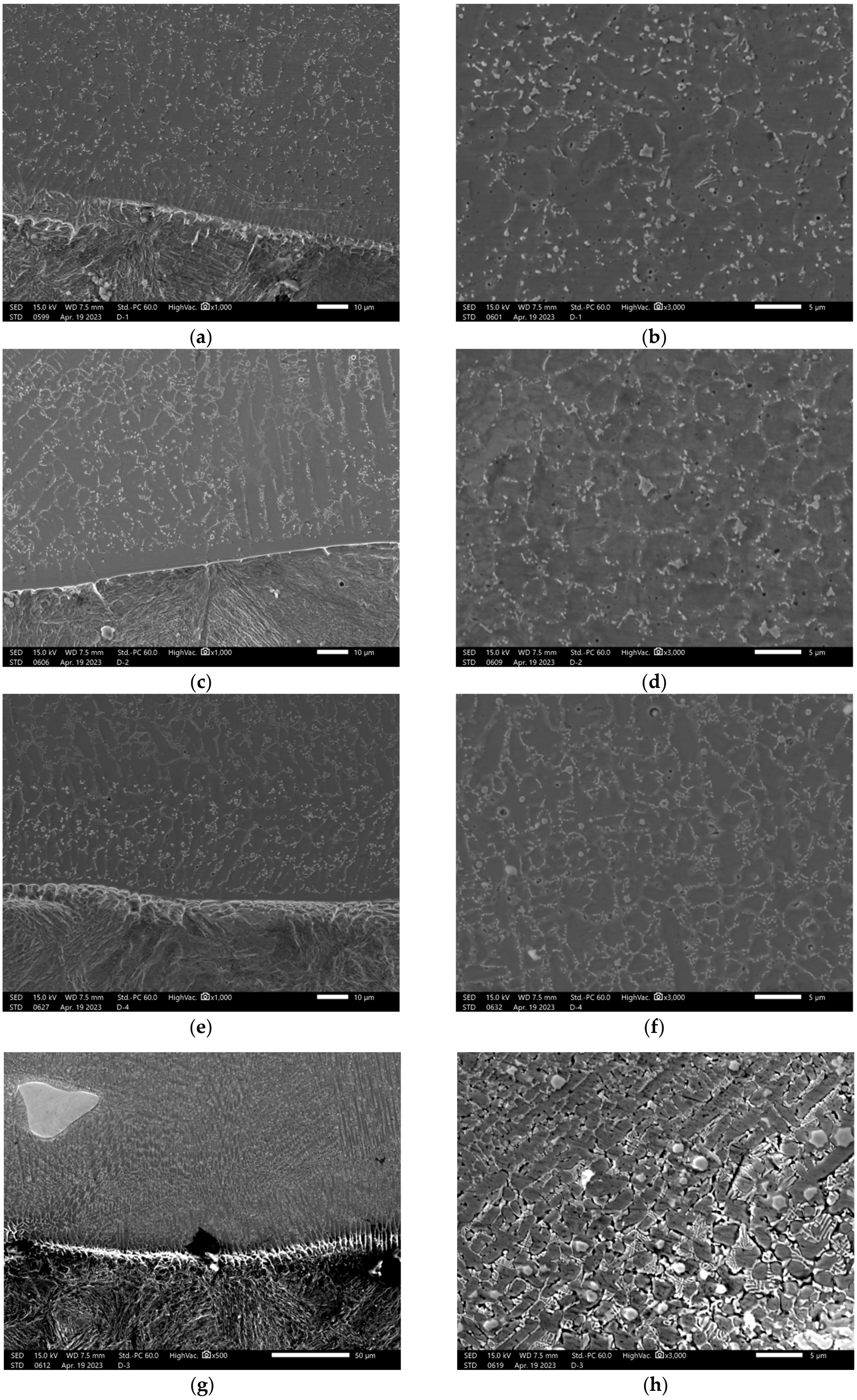

Figure 4. Microstructures of the composite coatings with different WC contents: (**a**,**b**) 10 wt.% WC; (**c**,**d**) 20 wt.% WC; (**e**,**f**) 30 wt.% WC; and (**g**,**h**) 40 wt.% WC.

3.2. Phase Composition

Figure 5 shows the XRD patterns of the coatings with different contents of WC added. All coatings were found to contain γ-(Fe,Ni), WC, W_2C, $M_{23}C_6$, and M_7C_3 phases, indicating the successful embedding of WC particles into the WC nickel-based coating. The diffraction peaks of γ-(Fe,Ni) grains in the D1 laser-cladded layer were the highest and narrowest. On the other hand, the diffraction peaks of the γ-(Fe,Ni) grains in the D4 laser-cladded layer were weaker and broader, indicating a finer coating structure. It can also be observed that as the WC content increased, the diffraction peaks became weaker and broader, indicating the strengthening effect of the fine crystalline structure with the addition of WC. These findings are consistent with the microstructure observations.

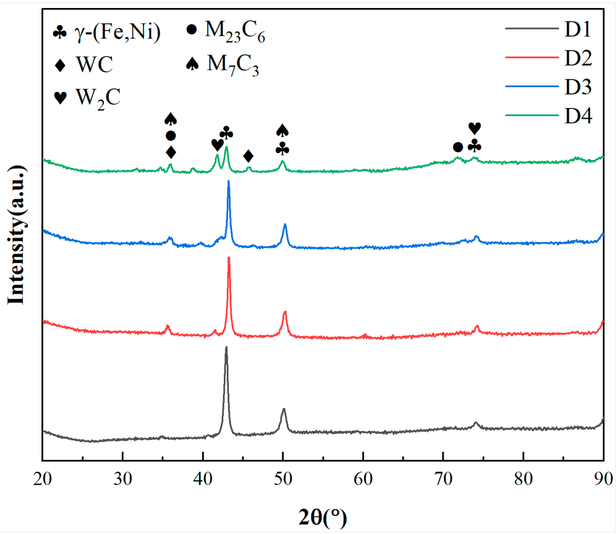

Figure 5. X-ray diffraction patterns of D1, D2, D3 and D4.

3.3. Microhardness

Figure 6 shows the surface hardness map of laser-cladded layers with different WC contents. From the hardness map, it can be observed that the coating with a 10% WC content had the lowest hardness, with a value of only 290.24 HV. As the WC content increased, the hardness of the coating gradually increased. When the WC content reached 40%, the average hardness could reach 474.8 HV, indicating that an increase in WC content can enhance the hardness of the laser-cladded layer. This can be attributed to the following reasons: Firstly, WC particles themselves are very hard (around 2600 HV) and do not completely dissolve in the composite coating, maintaining a better reinforcement effect. Secondly, as some WC particles dissolve in the matrix phase, they contribute to the solid solution strengthening of the matrix, thereby increasing the microhardness of the laser-cladded layer. Finally, with an increase in WC content, the grain structure of the laser-cladded layer becomes finer, resulting in increased grain-boundary strengthening and the improved microhardness of the laser-cladded layer [39].

3.4. Wear Property

Figure 7 shows the friction coefficient curves of laser-cladded layers with different WC contents, and Figure 8 presents the calculated average friction coefficients. From Figure 6, it can be observed that the friction coefficient curves under different WC contents exhibit a stable fluctuation trend within a certain range, but with varying initial steepness levels. It is worth noting that the friction coefficients of the specimens may experience sudden changes in some cases, and the friction coefficients of coatings often show peaks or valleys over time. This is because during the friction and wear process of the coatings, the complex and uneven distribution of the coating composition leads to different local microstructures and friction coefficients [40]. Therefore, when the Si_3N_4 ball friction passes through these regions, sudden changes in the friction coefficient occur. The uneven distribution of W elements and residual WC particles caused by the addition of WC particles also exacerbate this phenomenon of friction coefficient variation [41]. After 20 min, the friction coefficient of the sample with a 10 wt.% WC content fluctuated steadily between 0.3 and 0.4, with an average friction coefficient of 0.432. The coating of the sample with 20 wt.% WC content exhibited the highest friction coefficient, eventually fluctuating between 0.4 and 0.5, with an average friction coefficient of 0.447. The friction coefficient of the sample with 30 wt.% WC content fluctuated steadily between 0.3 and 0.4, with an average friction coefficient of 0.361. The friction coefficient of the sample with 40 wt.% WC content fluctuated steadily between 0.2 and 0.4, with an average friction coefficient of 0.335. This is consistent with previous findings by Hu et al. [42], where the addition of WC showed a trend of initially increasing and then decreasing the friction coefficient. This is mainly attributed to the fact that at a low WC content, the melting damage of some WC particles leads to an increase in friction coefficient. As the WC content increases, there are numerous small-sized WC particles present in the coating, as shown in Figure 4g,h. Relevant studies have confirmed that small-sized WC particles have a more pronounced anti-friction effect compared to larger-sized WC particles. Therefore, as the WC content increases, the friction coefficient decreases. Overall, it can be observed that an increase in WC content leads to a certain degree of reduction in the average friction coefficient.

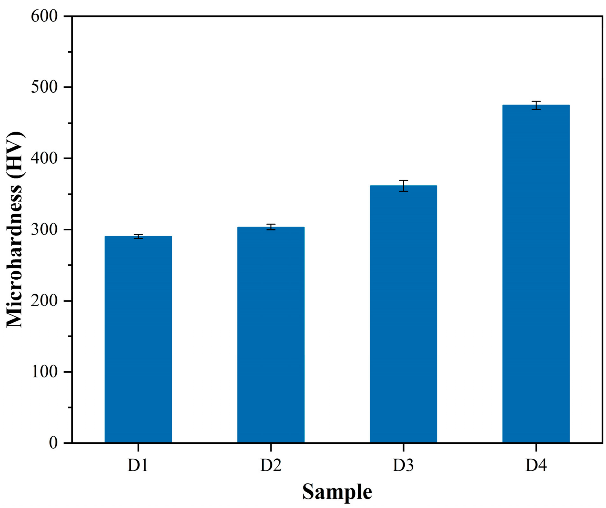

Figure 6. Comparison of the average microhardness of laser-cladded layers with different WC contents.

Figure 9 illustrates the variations in the wear volume and wear percentage of samples with different WC contents in friction and wear experiments. Consistent with the friction coefficient patterns, all four samples showed varying degrees of wear reduction. When the WC content was 10%, the wear percentage was 0.562%. When the WC content was 20%, the wear percentage was 0.556%. The sample with a WC content of 30% exhibited the greatest decrease in wear percentage, at 0.249%, and the coating with 40 wt.% WC had the lowest wear percentage, approximately 0.142%. Moreover, as the WC content increased, the wear volume of the samples steadily decreased from 18.5 mg to 4 mg, and the wear percentage decreased from 0.671% to 0.142%. Therefore, an increase in WC content can significantly enhance the wear resistance of nickel-based alloy coatings. The enhancement of wear resistance in the composite coating is attributed to the addition of WC, which alters the microstructure and increases the microhardness of the coating, similar to that found in previous research [43,44].

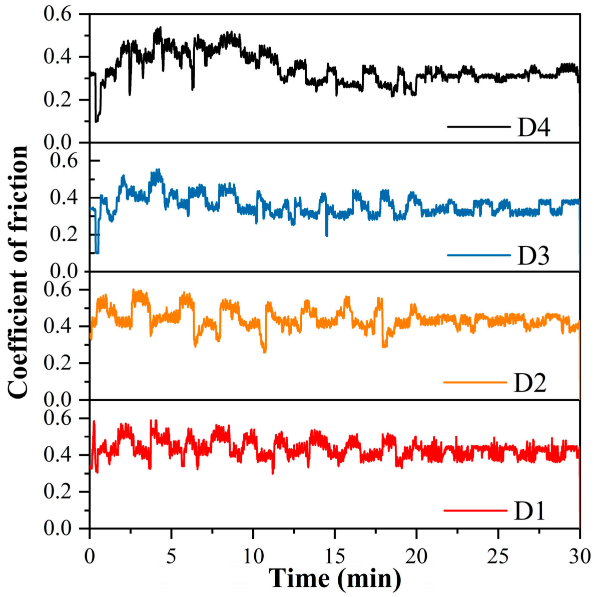

Figure 7. Curves of friction coefficient of laser-cladded layers with different WC contents.

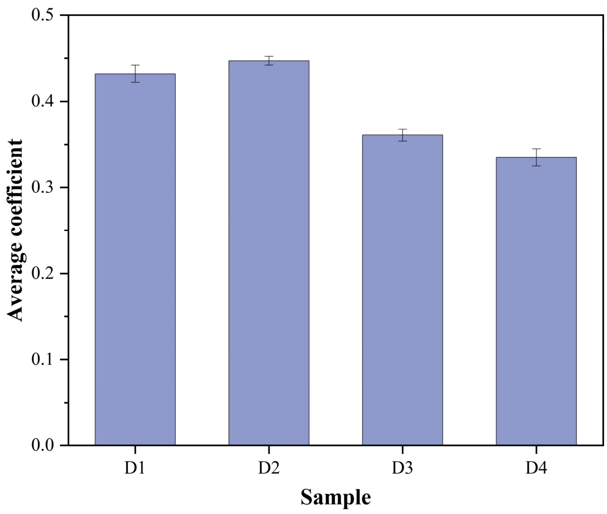

Figure 8. Average friction coefficients of laser-cladded layers with different WC contents.

In order to observe the wear mechanism, the wear tracks of the coating with 20 wt.% WC were captured using SEM. By observing Figure 10, it can be found that the coating wear track is relatively smooth, with some debris and spalling on the surface. Additionally, the coating exhibits a few scattered molten particles and evident furrows on the wear track surface. This can be attributed to the relatively high hardness of the friction Si_3N_4 ball and the lower hardness of the coating. During the wear process, the plastic deformation caused by the frictional force of the small ball on the coating was significant, resulting in the formation of block-like spalling regions on the coating surface. Simultaneously, as the wear process progressed, the spalling material was squeezed to form new wear debris, intensifying the surface wear of the coating. Furthermore, direct contact between the small ball and the coating led to adhesion wear, as the coating material adhered to the Si_3N_4 ball. Therefore, it is inferred that the main wear mechanisms of the laser-cladded layer are abrasive wear and adhesive wear [45].

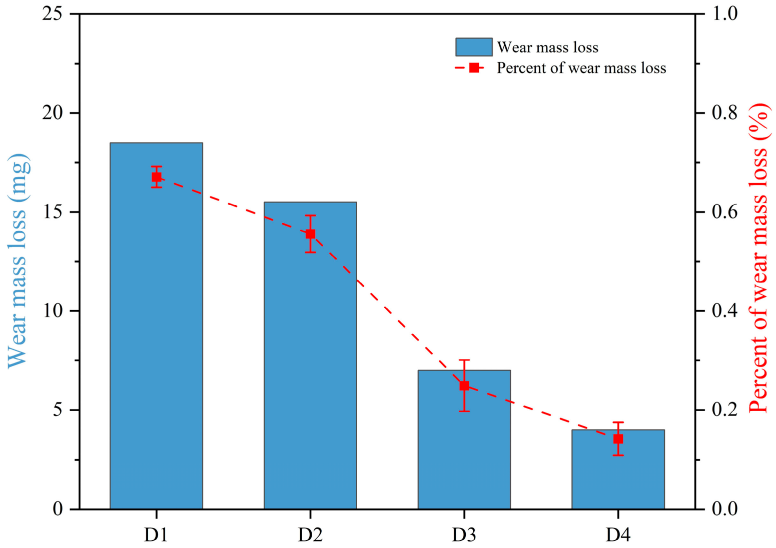

Figure 9. Wear mass loss and percentage of wear mass loss of laser-cladded layers with different WC contents.

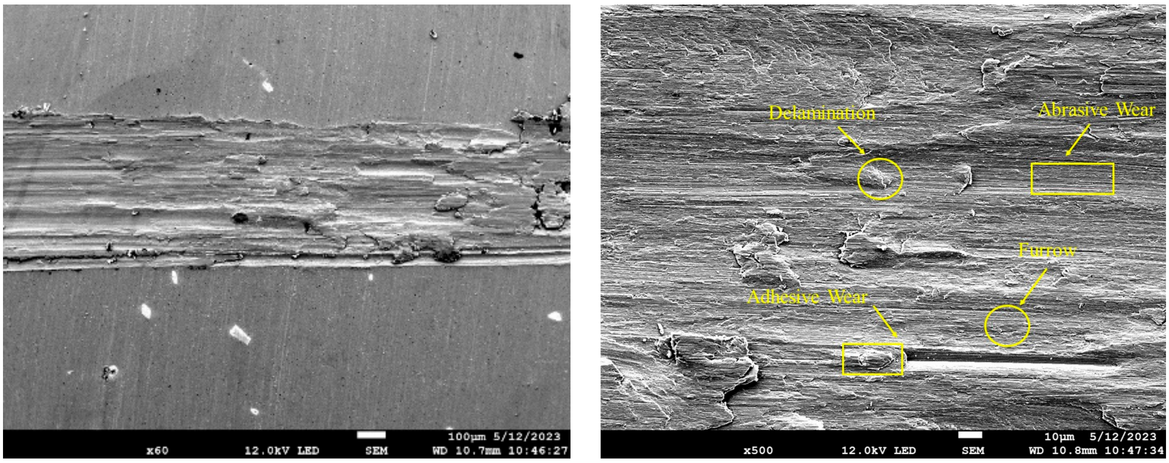

(**a**) (**b**)

Figure 10. Surface morphology of worn coating under different magnifications: (**a**) low magnification; (**b**) high magnification.

Scanning analysis of element distribution was conducted on the worn surface, as shown in Figure 11. It was observed that the proportion of oxygen elements was significantly higher than other elements, indicating the presence of oxidation wear [46]. In conclusion, it can be inferred that the laser-cladded layer has a fine and dense microstructure, ensuring both improved hardness and good wear resistance. During the wear process, the hard phases, such as carbides, distributed on the coating surface play a lubricating and supporting role [47]. Moreover, the predominant wear mechanisms of the coating are abrasive wear and oxidation wear, and the wear condition is relatively favorable.

3.5. Electrochemical Property

Figure 12 shows the open circuit potential (OCP) curves of four sample groups. From the graph, it can be observed that all four samples reached a steady state after fluctuations. The laser-cladded layers with different percentages of WC content gradually stabilized at −0.65 V, −0.39 V, −0.45 V, and −0.46 V, after an initial stage of continuous rise and fluctuations. This preliminarily indicates that the WC content can alter the corrosion tendency under electrochemical corrosion conditions. OCP, as a thermodynamic parameter, can preliminarily characterize the corrosion tendency of the sample in the corrosive medium.

However, it is necessary to combine the results of impedance spectroscopy and polarization curves for a comprehensive assessment.

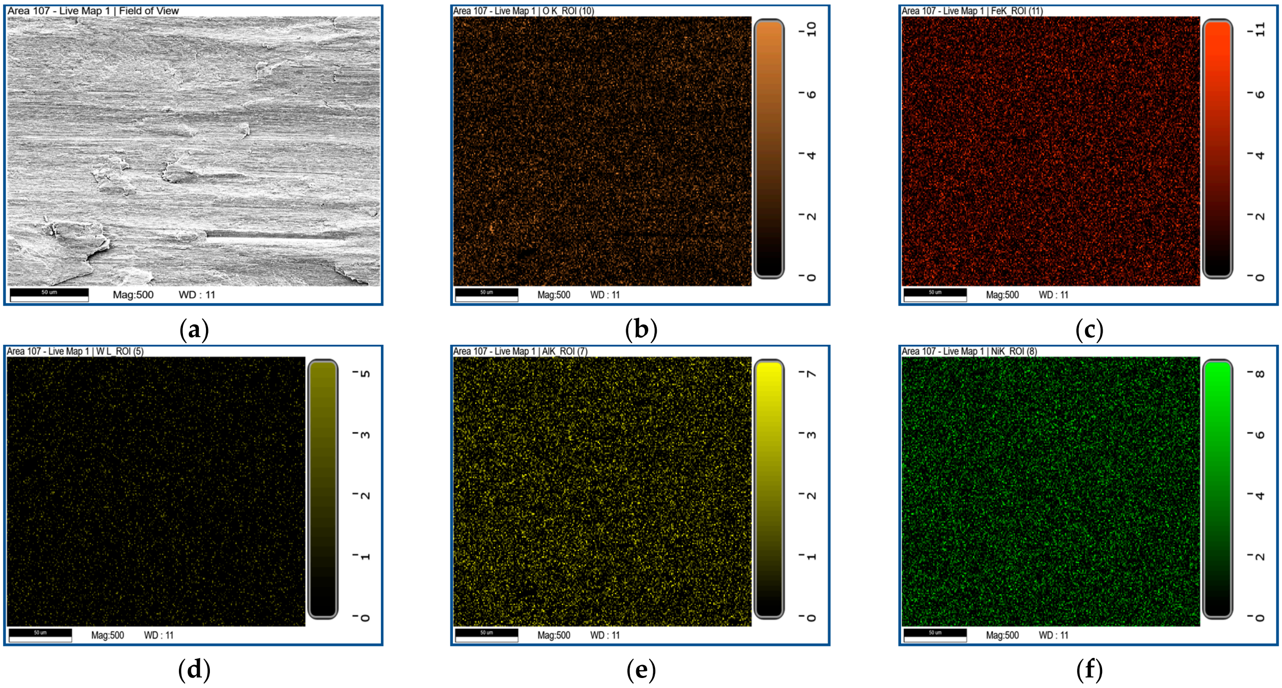

Figure 11. EDS mapping of the worn coating with 20 wt.% WC (**a**) wear surface: (**b**) O; (**c**) Fe; (**d**) W; (**e**) Al; (**f**) Ni.

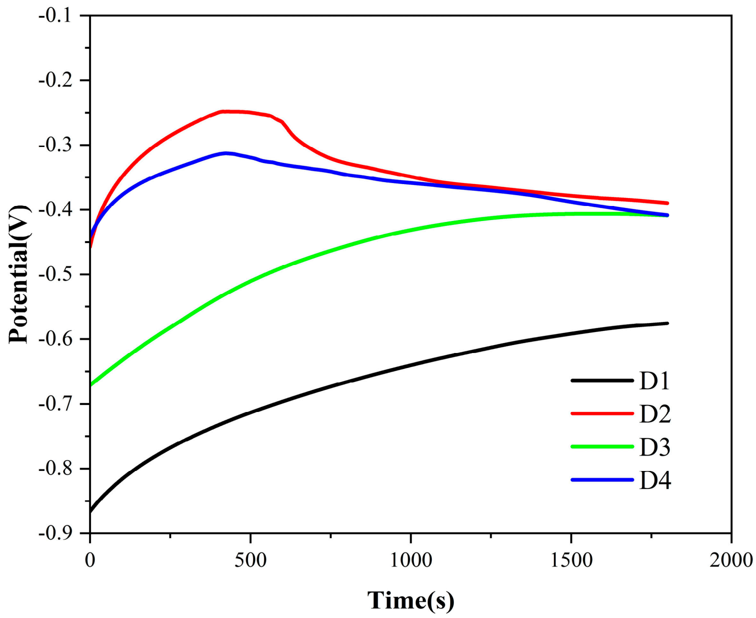

Figure 12. OCP curves of laser-cladded layers with different WC contents.

Figure 13 presents the polarization curves of the laser-cladded layers with different WC contents. The self-corrosion potential and corrosion current density of the samples were calculated based on these polarization curves, as shown in Table 3. In the potentiodynamic polarization curves, the corrosion potential (Ecorr) represents the tendency of an electrochemical reaction between the metal and corrosive medium in the environment, and the current density (Icorr) represents the electrochemical reaction rate. A higher Ecorr and lower Icorr in the polarization curves indicate better corrosion resistance. As shown in Table 3, the Ecorr and Icorr of the coating with 10 wt.% WC content are −0.753 V_{SCE} and 5.671 μA/cm^2, respectively. With the addition of WC, the curves moves towards an increase in Ecorr and a decrease in Icorr. Specifically, the coating with 20 wt.% WC content exhibited the highest corrosion potential (−0.472 V_{SCE}), and its current density (4.769 μA/cm^2) was 16% lower than that of the coating with 10 wt.% WC content. Furthermore, the further introduction of tungsten (W) resulted in a lower Ecorr and higher Icorr compared to the coating with 20 wt.% WC, which is consistent with the trend of OCP. The previous corrosion results of similar coatings, as shown in Table 4, indicate that we obtained a lower corrosion current density compared to the experimental results of Liu et al. [26], suggesting that the coatings we prepared possessed better corrosion resistance. Additionally, all four curves exhibit a relatively stable region, suggesting that all samples underwent certain passivation reactions. It can be preliminarily inferred that carbides, such as the WC on the coating surface and corrosion products covering the coating surface, play a role in inhibiting corrosion, thereby causing passivation phenomena.

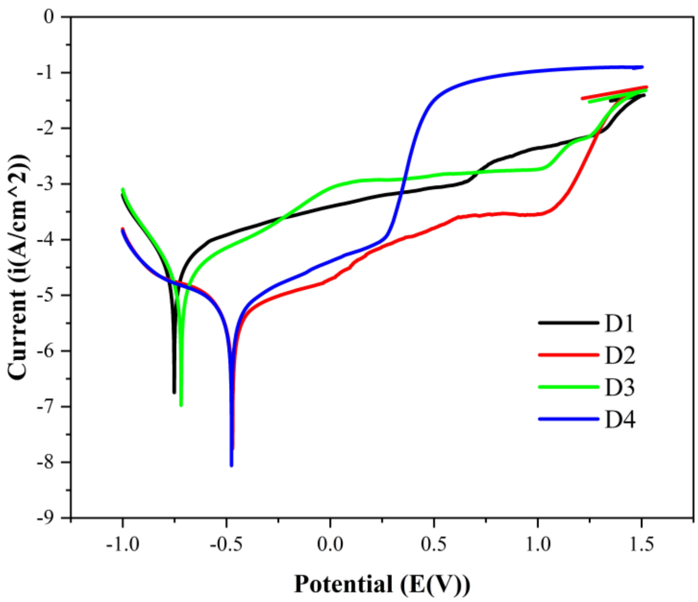

Figure 13. Potentiodynamic polarization curves of laser-cladded layers with different WC contents.

Table 3. Electrochemical parameters fitted by the potentiodynamic polarization curves.

Specimen	Ecorr (V_{SCE})	Icorr (μA/cm^2)
D-1	−0.753	5.671
D-2	−0.472	4.769
D-3	−0.718	5.600
D-4	−0.478	4.971

Table 4. Comparison of corrosion current densities in similar experiments (A/cm^2).

Our Experiment		Liu et al. Experiment [26]	
Sample	**Value**	**Sample**	**Value**
10 WC/Ni	5.671×10^{-6}	Ni	9.5×10^{-5}
20 WC/Ni	4.769×10^{-6}	10 WC/Ni	8.2×10^{-5}
30 WC/Ni	5.6×10^{-6}	20 WC/Ni	5.6×10^{-5}
40 WC/Ni	4.971×10^{-6}		

Figure 14 presents the Nyquist plots, Bode impedance plots, and equivalent circuit diagrams obtained through EIS measurements after immersing samples with different WC contents in a 3.5 wt.% NaCl electrolyte for 30 min. Essentially, the radius of the capacitive loop in the Nyquist plot is always associated with the corrosion resistance of the samples, with a larger radius indicating better corrosion resistance. As shown in Figure 14a, all curves consist of capacitive loops ranging from high frequency (10^5 Hz) to low frequency (10^{-2} Hz), and the curve of the coating with a 20 wt.% WC content exhibited the largest capacitive loop diameter, indicating the best corrosion resistance with an addition of 20 wt.% WC. Additionally, the impedance modulus |Z| at a low frequency is also related to the corrosion resistance. As shown in Figure 14b, |Z| results indicate that the lead-in W enhances the corrosion resistance of the coating. As shown in Figure 14c, each curve of the phase angle has a peak in the intermediate frequency range (10^0–10^3 Hz). However, with the doping of WC, the width of the peak decreases, with the coating containing 20 wt.% WC having the widest peak, and its phase angle remained relatively stable in the frequency range of 10^{-2} to 10^{-1} Hz, eventually reaching 63.014°. In order to further quantitatively study the impedance spectroscopy data of the samples, the corresponding equivalent circuit diagram (Figure 14d) was used to fit the data. RS represents the resistance of 3.5 wt.% NaCl solution between the working electrode and reference electrode, RL represents the resistance of the thin passivation film formed on the surface of the coating during EIS measurements, and Rct corresponds to the electron-transfer resistance between the coating and NaCl solution. Inductance (L), capacitance (C), and the constant phase element (CPE) were used to describe the behavior of non-ideal electrical double-layer capacitors. All four groups of samples were analyzed using the LR(CR)(QR) circuit, with Rct chosen to represent the resistance of the specimen [48]. From the results in Table 5, it can be seen that the charge transfer resistance (Rct) of the WC-added overlay coatings first increases and then decreases, with the 20 wt.% WC coating reaching 2.213×10^4 Ω, which was 17.52, 10.59, and 3.10 times that of the other samples, respectively. A larger R_{ct} value indicates a slower charge transfer in the coating; thus, the 20 wt.% WC coating exhibited better corrosion resistance compared to the other samples. For this sample, the improvement in corrosion resistance is mainly attributed to the reformation of fine carbides at the coating grain boundaries, which block the corrosion channels, and a more uniform distribution of elements, which promotes the growth of the passivation film. The impedance analysis and polarization results are consistent with each other, indicating that increasing WC content can enhance the corrosion resistance of a coating.

Table 5. EIS fitting results in equivalent circuit diagrams.

Specimen	L	R_s	C	R_L	CPE		R_{ct}
	(μH)	**(Ω·cm²)**	**(F)**	**(Ω·cm²)**	Y_O **(F/cm²)**	n	**(Ω·cm²)**
D-1	0.6981	9.315	1.390×10^{-2}	1007	1.060×10^{-3}	0.6284	1.216×10^3
D-2	0.6802	9.995	2.985×10^{-4}	24.89	8.762×10^{-5}	0.7352	2.213×10^4
D-3	0.7030	8.586	9.787×10^{-4}	141.4	1.849×10^{-3}	0.5421	2.012×10^3
D-4	0.6835	9.086	7.515×10^{-4}	5364	5.881×10^{-5}	0.8473	6.882×10^3

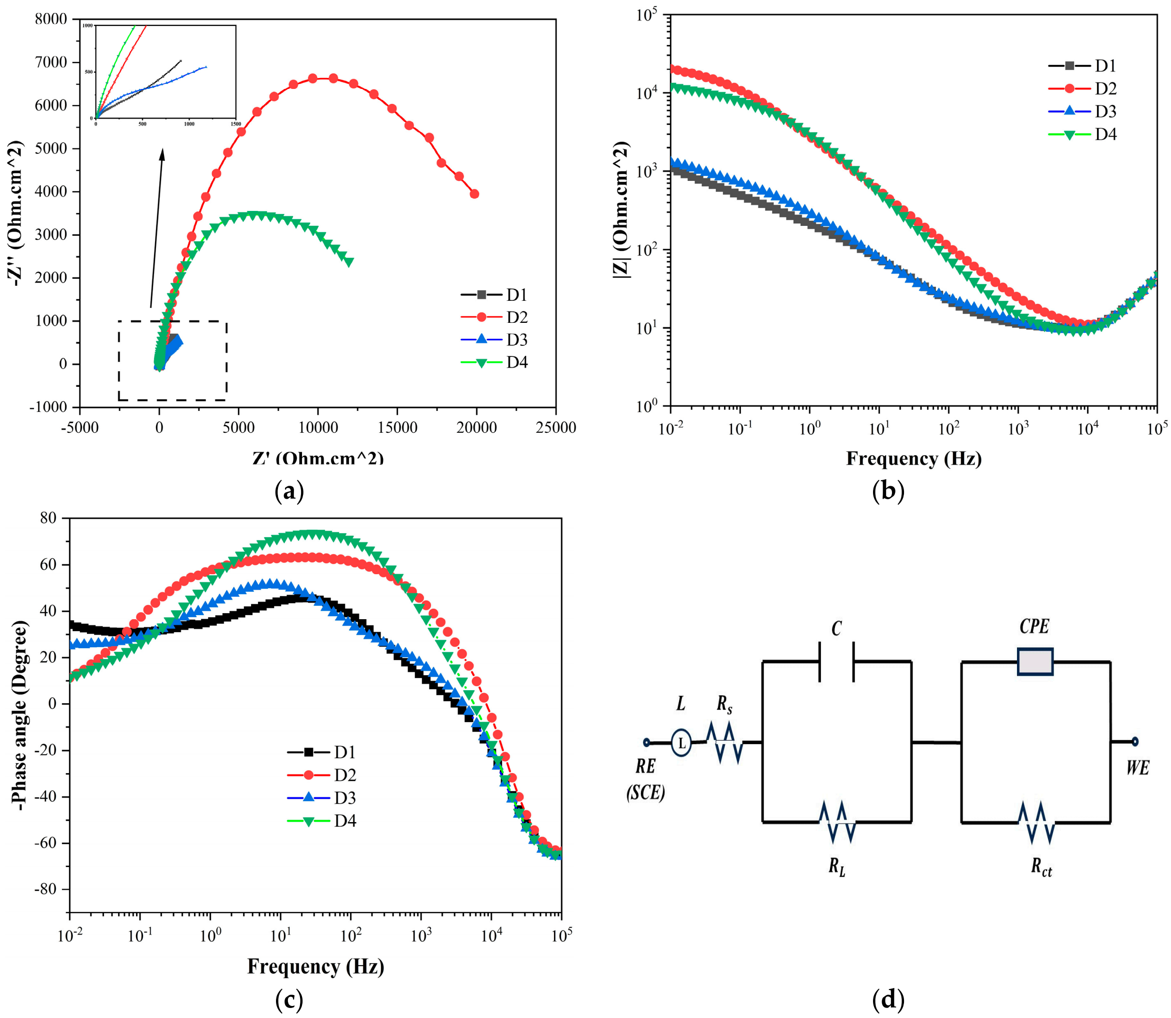

Figure 14. (**a**) Nyquist plots, (**b**) Bode impedance plots, (**c**) phase angle, and (**d**) equivalent circuit diagram for the D1, D2, D3 and D4 coatings.

4. Conclusions

The selected overlay material for this experiment was nickel-based powder with a varying WC content. The microstructure and properties of the coatings prepared with different WC contents were systematically studied. The main conclusions of this study are as follows:

(1) The microstructure of the oscillating laser-cladded layer gradually transforms from the plane crystal and cellular crystal at the bottom to the columnar crystal and equiaxed crystal at the top. With an increase in WC content, the fine grains formed in the laser-cladded layer become more and more uniform.

(2) With an increase in WC content, the hardness of a coating gradually increases. When the WC content reaches 40%, the average hardness can reach 474.8 HV.

(3) The friction coefficient curve decreases with an increase in WC content. A 40 wt.% WC content, a coating exhibits the best wear resistance, and the main wear mechanisms are abrasive wear and oxidative wear.

(4) When the WC content is 20%, the oscillating laser-cladded layer exhibits the best corrosion resistance in a 3.5 wt.% NaCl solution, with a polarization resistance 16% lower than that of the cladding layer with a WC content of 10%.

Author Contributions: Conceptualization, formal analysis and writing—original draft, X.L., S.Z. and K.W.; writing—original draft preparation, X.L., S.Z. and W.L.; methodology, data curation and funding acquisition, K.W. and M.Z.; project administration and supervision, K.W.; data analysis, writing—review and editing, X.P., Y.T., M.Z. and J.Z. All authors have read and agreed to the published version of the manuscript.

Funding: The authors would like to acknowledge the financial support for this work from the National Natural Science Foundation of China (52205334), the Natural Science Foundation of Hunan Province (2022JJ40495), the Changsha Municipal Natural Science Foundation (kq2202196), the Changsha Key Research and Development Project (kh2201275), and the Tribology Science Fund of the State Key Laboratory of Tribology in Advanced Equipment (SKLTKF21B08).

Institutional Review Board Statement: Not applicable.

Informed Consent Statement: Not applicable.

Data Availability Statement: Not applicable.

Conflicts of Interest: The authors declare no conflict of interest.

References

1. Mandal, R.; Maity, T. Operational process parameters of underground coal gasification technique and its control. *J. Process Control* **2023**, *129*, 103031. [CrossRef]
2. Zhou, H.; Zhang, Y.; Ma, H.; Lei, Y.; Yang, Z.; Zhao, H.; Gao, Y.; Zhu, K. Inhibition of the erosion-corrosion of elbow by synergistic action of swirling flow and inhibitor. *Wear* **2023**, *514–515*, 204570. [CrossRef]
3. Zdravecká, E.; Slota, J.; Tkáčová, J. Erosive failure of steel pipeline by solid pulverized particles. *Eng. Fail. Anal.* **2014**, *46*, 18–25. [CrossRef]
4. Li, Y.; Wang, K.; Fu, H.; Guo, X.; Lin, J. Microstructure and wear resistance of in-situ TiC reinforced AlCoCrFeNi-based coatings by laser cladding. *Appl. Surf. Sci.* **2022**, *585*, 152703. [CrossRef]
5. Wang, K.; Liu, W.; Hong, Y.; Du, D.; Chang, B.; Tong, Y.; Hu, Y.; Ji, X.; Ju, J. Effect of solution cooling rates on microstructure and mechanical properties of K648 high chromium superalloy additive-manufactured by the extreme high-speed laser metal deposition. *J. Mater. Res. Technol.* **2023**, *24*, 8391–8400. [CrossRef]
6. Jin, M.; He, D.; Shao, W.; Tan, Z.; Cao, Q.; Guo, X.; Zhou, Z.; Cui, L.; Zhou, L. The microstructure and high-temperature oxidation resistance of Si-rich Mo-Si-B coatings prepared by ultrasonic vibration assisted laser cladding. *J. Alloys Compd.* **2023**, *953*, 170175. [CrossRef]
7. Chen, C.; Feng, A.; Wei, Y.; Wang, Y.; Pan, X.; Song, X. Effect of multiple laser shock peening on the microstructure and properties of laser cladding nano-WC/Ni60 composite coatings. *Opt. Laser Technol.* **2023**, *167*, 109719. [CrossRef]
8. Zhu, Q.; Zhou, X.; Yang, F.; Ji, Y.; Kong, Y.; Bi, A.; Zhou, Z.; Wang, X.; Wang, R.; Zhang, Z.; et al. Microstructure formation, corrosion properties, and tribological properties of laser-cladded CrCoNi medium-entropy alloy coatings. *Mater. Lett.* **2023**, *347*, 134649. [CrossRef]
9. Zhang, F.; Qiu, Y.; Hu, T.; Clare, A.T.; Li, Y.; Zhang, L. Microstructures and mechanical behavior of beta-type Ti-25V-15Cr-0.2Si titanium alloy coating by laser cladding. *Mater. Sci. Eng. A* **2020**, *796*, 140063. [CrossRef]
10. Mostajeran, A.; Shoja-Razavi, R.; Hadi, M.; Erfanmanesh, M.; Barekat, M.; Savaghebi Firouzabadi, M. Evaluation of the mechanical properties of WC-FeAl composite coating fabricated by laser cladding method. *Int. J. Refract. Met. Hard Mater.* **2020**, *88*, 105199. [CrossRef]
11. Ding, H.; Cao, Y.; Hua, K.; Tong, Y.; Li, N.; Sun, L.; Li, X.; Wu, H.; Wang, H. Fretting wear resistance at ambient and elevated temperatures of 316 stainless steel improved by laser cladding with Co-based alloy/WC/CaF_2 composite coating. *Opt. Laser Technol.* **2023**, *163*, 109428. [CrossRef]
12. Xu, Y.; Wang, G.; Song, Q.; Lu, X.; Li, Z.; Zhao, Q.; Chen, Y. Microstructure, mechanical properties, and corrosion resistance of SiC reinforced $Al_xCoCrFeNiTi_{1-x}$ high-entropy alloy coatings prepared by laser cladding. *Surf. Coat. Technol.* **2022**, *437*, 128349. [CrossRef]
13. Bai, J.; Bu, G. Progress in 4D printing technology. *J. Adv. Manuf. Sci. Technol.* **2022**, *2*, 2022001. [CrossRef]
14. Soori, M.; Arezoo, B.; Dastres, R. Advanced virtual manufacturing systems: A review. *J. Adv. Manuf. Sci. Technol.* **2023**, *3*, 2023009. [CrossRef]
15. Guo, N.; Gao, Y.; Gao, Y.; Gu, X.; Liu, X.; Zhang, S.; Fu, Y. Microstructure and properties of in-situ nickel-aluminum bronze coating by underwater wire-feed laser cladding. *J. Mater. Res. Technol.* **2023**, *25*, 6459–6471. [CrossRef]
16. Hu, D.; Liu, Y.; Chen, H.; Wang, M. Microstructure and wear resistance of Ni-based tungsten carbide coating by laser cladding on tunnel boring machine cutter ring. *Surf. Coat. Technol.* **2020**, *404*, 126432. [CrossRef]
17. Shi, X.; Wen, D.; Wang, S.; Wang, G.; Zhang, M.; Li, J.; Xue, C. Investigation on friction and wear performance of laser cladding Ni-based alloy coating on brake disc. *Optik* **2021**, *242*, 167227. [CrossRef]

18. Li, X.; Zhang, C.H.; Zhang, S.; Wu, C.L.; Liu, Y.; Zhang, J.B.; Babar Shahzad, M. Manufacturing of Ti_3SiC_2 lubricated Co-based alloy coatings using laser cladding technology. *Opt. Laser Technol.* **2019**, *114*, 209–215. [CrossRef]
19. He, B.; Liu, X.; Zhang, F.; Zhang, S.; Liu, Z.; Zhang, S. Tribological and oxidation behaviors of TiN reinforced Co matrix composite coatings on Inconel718 alloy by laser cladding. *Tribol. Int.* **2023**, *188*, 108781. [CrossRef]
20. Rezaee Hajideh, M.; Farahani, M. Direct laser metal deposition cladding of IN718 on DIN 1.2714 tool steel reinforced by the SiC nanoparticles. *J. Mater. Res. Technol.* **2023**, *23*, 2020–2030. [CrossRef]
21. Sun, X.; Ren, X.; Qiang, W.; Feng, Y.; Zhao, X.; Huang, B. Microstructure and properties of Inconel 718 matrix composite coatings reinforced with submicron TiC particles prepared by laser cladding. *Appl. Surf. Sci.* **2023**, *637*, 157920. [CrossRef]
22. Shen, X.; Zhang, C.; Peng, H.; Liu, C.; Zhang, Y. Achieving high surface integrity of Fe-based laser cladding coating by optimized temperature field-assisted ultrasonic burnishing. *J. Manuf. Process.* **2022**, *83*, 270–280. [CrossRef]
23. Zhu, Z.; Li, J.; Peng, Y.; Shen, G. In-situ synthesized novel eyeball-like Al_2O_3/TiC composite ceramics reinforced Fe-based alloy coating produced by laser cladding. *Surf. Coat. Technol.* **2020**, *391*, 125671. [CrossRef]
24. Wu, S.; Liu, Z.; Gong, Y.; Liang, X.; Wu, Y.; Zhao, X. Analysis of the sequentially coupled thermal–mechanical and cladding geometry of a Ni60A-25 %WC laser cladding composite coating. *Opt. Laser Technol.* **2023**, *167*, 109595. [CrossRef]
25. Wu, T.; Shi, W.; Xie, L.; Gong, M.; Huang, J.; Xie, Y.; He, K. Study on the effect of Ni60 transition coating on microstructure and mechanical properties of Fe/WC composite coating by laser cladding. *Opt. Laser Technol.* **2023**, *163*, 109387. [CrossRef]
26. Liu, Y.; Gu, X.; Lou, C.; Kang, L.; Hou, Q.; Ma, C. Influence of WC ceramic particles on structures and properties of laser cladding Ni50-WC coatings. *J. Mater. Res. Technol.* **2023**, *26*, 14–21. [CrossRef]
27. Shu, X.; Wu, Y.; Zheng, J.; Shou, B. Experimental study on the minimum design metal temperature of Q345R steel. *J. Zhejiang Univ.-Sci. A* **2018**, *19*, 491–504. [CrossRef]
28. Deng, D.; Li, T.; Huang, Z.; Jiang, H.; Yang, S.; Zhang, Y. Multi-response optimization of laser cladding for TiC particle reinforced Fe matrix composite based on Taguchi method and grey relational analysis. *Opt. Laser Technol.* **2022**, *153*, 108259. [CrossRef]
29. Shu, L.; Li, J.; Wu, H.; Heng, Z. Optimization of Multi-Track Laser-Cladding Process of Titanium Alloy Based on RSM and NSGA-II Algorithm. *Coatings* **2022**, *12*, 1301. [CrossRef]
30. Fan, P.; Zhang, G. Study on process optimization of WC-Co50 cermet composite coating by laser cladding. *Int. J. Refract. Met. Hard Mat.* **2020**, *87*, 105133. [CrossRef]
31. Huang, Y.; Hu, Y.; Zhang, M.; Mao, C.; Wang, K.; Tong, Y.; Zhang, J.; Li, K. Multi-Objective Optimization of Process Parameters in Laser Cladding CoCrCuFeNi High-Entropy Alloy Coating. *J. Therm. Spray Technol.* **2022**, *31*, 1985–2000. [CrossRef]
32. Tang, B.; Tan, Y.; Zhang, Z.; Xu, T.; Sun, Z.; Li, X. Effects of Process Parameters on Geometrical Characteristics, Microstructure and Tribological Properties of TiB_2 Reinforced Inconel 718 Alloy Composite Coatings by Laser Cladding. *Coatings* **2020**, *10*, 76. [CrossRef]
33. Shi, B.; Mu, X.; Zhan, H.; Deng, L.; Li, T.; Zhang, H. Crack Behavior of Ni60A Coating Prepared by Laser Cladding on a Tilted Substrate. *Coatings* **2022**, *12*, 966. [CrossRef]
34. Zuo-Jiang, S.; Yu, H.; Jiang, X.; Gao, W.; Sun, D. A thermal field FEM of titanium alloy coating on low-carbon steel by laser cladding with experimental validation. *Surf. Coat. Technol.* **2023**, *452*, 129113. [CrossRef]
35. Dong, H.; Guo, P.; Han, Y.; Bai, R.; Yang, Z.; Zhang, S. Enhanced corrosion resistance of high speed laser-cladded Ni/316L alloy coating by heat treatment. *J. Mater. Res. Technol.* **2023**, *24*, 952–962. [CrossRef]
36. Zhang, K.; Ju, H.; Xing, F.; Wang, W.; Li, Q.; Yu, X.; Liu, W. Microstructure and properties of composite coatings by laser cladding Inconel 625 and reinforced WC particles on non-magnetic steel. *Opt. Laser Technol.* **2023**, *163*, 109321. [CrossRef]
37. Lv, G.; Yang, X.; Gao, Y.; Wang, S.; Xiao, J.; Zhang, Y.; Chen, K.; Yang, H. Investigation on fretting Wear performance of laser cladding WC/Co06 coating on 42CrMo steel for hydraulic damper. *Int. J. Refract. Met. Hard Mater.* **2023**, *111*, 106068. [CrossRef]
38. Wang, J.; Zhou, J.; Zhang, T.; Meng, X.; Li, P.; Huang, S.; Zhu, H. Ultrasonic-Induced Grain Refinement in Laser Cladding Nickel-Based Superalloy Reinforced by WC Particles. *Coatings* **2023**, *13*, 151. [CrossRef]
39. Li, T.; Long, H.; Qiu, C.; Wang, M.; Li, D.; Dong, Z.; Gui, Y. Multi-Objective Optimization of Process Parameters of 45 Steel Laser Cladding Ni60PTA Alloy Powder. *Coatings* **2022**, *12*, 939. [CrossRef]
40. Nian, L.; Wang, M.; Ge, X.; Wang, X.; Xu, Y. Thermo-Mechanical Coupling Numerical Simulation for Extreme High-Speed Laser Cladding of Chrome-Iron Alloy. *Coatings* **2023**, *13*, 879. [CrossRef]
41. Lv, J.; Zhou, J.; Zhang, T.; Meng, X.; Li, P.; Huang, S. Microstructure and Wear Properties of IN718/WC Composite Coating Fabricated by Ultrasonic Vibration-Assisted Laser Cladding. *Coatings* **2022**, *12*, 412. [CrossRef]
42. Hu, Z.; Li, Y.; Lu, B.; Tan, N.; Cai, L.; Yong, Q. Effect of WC content on microstructure and properties of high-speed laser cladding Ni-based coating. *Opt. Laser Technol.* **2022**, *155*, 108449. [CrossRef]
43. Gao, Y.; Chen, H.; Zhou, J.; Tian, W.; Nie, H.; Wang, W.; Liang, J. Microstructures and wear behaviors of WC particle reinforced nickel-based composites fabricated by selective laser melting. *J. Manuf. Process.* **2023**, *95*, 291–301. [CrossRef]
44. Wang, W.; Cai, Z.; Li, S.; Wang, D.; Li, Y.; Luo, D.; Wu, D.; Fan, X.; Yamaguchi, T. Microstructure and wear resistance of in-situ synthesized stellate Mo2C reinforced WC/amorphous composite coatings by resistance seam welding (RSW). *Tribol. Int.* **2023**, *186*, 108599. [CrossRef]
45. Wang, K.; Liu, W.; Hong, Y.; Sohan, H.M.S.; Tong, Y.; Hu, Y.; Zhang, M.; Zhang, J.; Xiang, D.; Fu, H.; et al. An Overview of Technological Parameter Optimization in the Case of Laser Cladding. *Coatings* **2023**, *13*, 496. [CrossRef]

46. Du, L.M.; Lan, L.W.; Zhu, S.; Yang, H.J.; Shi, X.H.; Liaw, P.K.; Qiao, J.W. Effects of temperature on the tribological behavior of Al0.25CoCrFeNi high-entropy alloy. *J. Mater. Sci. Technol.* **2019**, *35*, 917–925. [CrossRef]
47. Xue, J.; Guo, W.; Yang, J.; Xia, M.; Zhao, G.; Tan, C.; Wan, Z.; Chi, J.; Zhang, H. In-situ observation of microcrack initiation and damage nucleation modes on the HAZ of laser-welded DP1180 joint. *J. Mater. Sci. Technol.* **2023**, *148*, 138–149. [CrossRef]
48. Sun, P.; Wang, D.; Song, W.; Tang, C.; Yang, J.; Xu, Z.; Hu, Q.; Zeng, X. Influence of W content on microstructure and corrosion behavior of laser cladded Inconel 718 coating. *Surf. Coat. Technol.* **2023**, *452*, 129079. [CrossRef]